Energy & Environmental Science

ROYAL SOCIETY OF CHEMISTRY

COMMUNICATION

View Article Online
View Journal | View Issue



Check for updates

Cite this: *Energy Environ. Sci.*, 2022, **15**, 3805

Received 29th April 2022,
Accepted 25th July 2022

DOI: 10.1039/d2ee01390h

rsc.li/ees

# Interfacial modification between argyrodite-type solid-state electrolytes and Li metal anodes using LiPON interlayers†

Jin Su, *[ab] Mauro Pasta,[ab] Ziyang Ning,[ab] Xiangwen Gao,[ab] Peter G. Bruce[ab] and Chris R. M. Grovenor*[ab]

**Solid-state batteries (SSBs) using lithium (Li) metal anodes and solid-state electrolytes (SSEs) can offer both improved energy densities and, by removing flammable liquid electrolytes, improved safety. The argyrodite-type $Li_6PS_5Cl$ ceramic is an attractive candidate SSE material because of its high ionic conductivity (>1 mS cm$^{-1}$) at room temperature and relatively ductile mechanical properties. However, interface contact issues between the SSE and Li metal hamper the practical development of solid-state Li metal batteries. In this work, we show that the interfacial resistance between the $Li_6PS_5Cl$ SSE and Li metal anode can be reduced to as low as 1.3 Ω cm$^2$ in symmetric cells by introducing a thin amorphous and Li-ion conducting lithium phosphorus oxynitride (LiPON) interlayer. We demonstrate that this interlayer improves the wetting behaviour of the $Li_6PS_5Cl$ SSE, and helps form an effective conformal interfacial contact between the $Li_6PS_5Cl$ SSE and Li metal. LiPON coated $Li_6PS_5Cl$ symmetric cells with reduced interfacial resistance exhibit stable Li plating/stripping cycling for over 1000 h at 0.5 mA cm$^{-2}$, and a dramatically improved critical current density of 4.1 mA cm$^{-2}$ at 30 °C. These results demonstrate a reliable thin-film coating strategy for improving contact between the SSEs and Li metal anodes, stabilizing interfaces and realizing the practical application of solid-state Li metal batteries.**

### Broader context

All-solid-state batteries are considered to be a promising technology to give long-lasting products with both higher energy densities and better safety than conventional batteries based on liquid electrolytes. However, a challenge for the practical development of SSBs with Li metal anodes is their high interfacial resistance due to the poor wettability of the SSEs with Li metal, which leads to poor contacts, inhomogeneous ion diffusion and current density hotspots between the SSE and the Li metal. The ideal interphase between SSEs and Li metal anodes should have an acceptable value of Li-ion conductivity, low electronic conductivity and chemical stability with Li metal. Our research demonstrates that introducing a thin amorphous LiPON interlayer with a well-controlled ionic conductivity can play an important role in stabilizing the interfaces between SSEs and Li metal, both chemically and mechanically, and results in low interfacial impedance. This excellent performance of LiPON coated $Li_6PS_5Cl$ SSE based symmetric cells can be attributed to homogenous Li plating/stripping processes encouraged by the LiPON interlayers.

Lithium metal is considered to be one of the most promising anode materials for lithium-ion batteries because it gives theoretical gravimetric (3860 mA h g$^{-1}$) and volumetric (2046 mA h cm$^{-3}$) capacities, much greater than achieved with graphite anodes (372 mA h g$^{-1}$, 719 mA h cm$^{-3}$).[1–3] However, Li dendrite growth and the formation of solid electrolyte interphase (SEI) layers in liquid organic electrolytes leads to safety issues and a reduction in battery life, and has limited the widespread application of Li metal anodes for traditional commercial rechargeable batteries.[4,5] Solid-state batteries (SSBs) containing Li metal anodes and ceramic solid-state electrolytes (SSEs) have the potential both to generate higher specific capacity and offer better safety than Li-ion batteries with flammable organic electrolytes, and are thus being considered for wide usage in electric vehicles and the storage of electricity generated from intermittent renewable wind and solar energy.[6–11] SSEs with fast ion conductivity may have the potential to delay lithium dendrite growth and thereby enable the practical application of Li metal anodes.[6] Even if dendrite growth cannot be avoided, leading to the eventual failure of solid-state batteries by short circuiting, the non-flammable nature of the solid electrolyte can avoid the risk of fires and explosions.

A considerable body of research has explored the development of fast Li-ion conducting SSEs, including sulphide,[12,13] garnet,[14] perovskite[15] and LISICON[16] materials, *etc.* Among

[a] *Department of Materials, University of Oxford, Parks Road, Oxford, OX1 3PH, UK. E-mail: chris.grovenor@materials.ox.ac.uk, jin.su@materials.ox.ac.uk*
[b] *The Faraday Institution, Quad One, Becquerel Avenue, Harwell Campus, Didcot, OX11 0RA, UK*

† Electronic supplementary information (ESI) available. See DOI: https://doi.org/10.1039/d2ee01390h

these SSEs, the argyrodite $Li_6PS_5Cl$ solid-state electrolyte has attracted great interest because of its high ionic conductivity ($>1$ mS cm$^{-1}$) at room temperature, less brittle mechanical properties compared with other oxide and sulphide SSE compounds, ease of synthesis, and low-temperature fabricability, all of which are crucial requirements for scalable application of SSBs.[17–19] However, argyrodite $Li_6PS_5Cl$ is not chemically nor electrochemically stable in contact with Li metal, and decomposes to an insulating interphase layer containing several Li compounds.[19] A challenge for the practical development of SSBs with Li metal anodes is their high interfacial resistance because of the poor wetting of the SSEs with heated Li metal, which gives rise to loose contacts, inhomogeneous ion diffusion and localized current density hotspots between SSEs and the Li metal.[20–23] Plenty of research has attempted to improve the interfacial contact and reduce the impedance between the SSEs and Li metal, including surface coating of SSEs by various materials like Si,[20] Ge,[21] $Cu_3N$[22] and $Li_3N$,[23] and these approaches have indeed improved the wetting behaviour of ceramic SSEs. In particular, by appropriate choice of the coating material, the chemical properties of the SSEs surface can be changed from lithiophobic to lithiophilic.[20–23] However, most of these improvements still only result in successful cycling at small current densities at room temperature, far below the practical high current densities ($>1.0$ mA cm$^{-2}$) required for SSBs application.[20–24] Fast charging is considered to be a crucial requirement for the widespread adoption of battery-driven electric vehicles,[25] and this requires SSBs that can withstand operation at these high current densities. This limitation in current density can be attributed to the gradual increase in interfacial impedance between SSEs and Li metal because of unstable interphase changes and contact loss during Li plating/stripping.[26] The ideal interphase between SSEs and Li metal electrodes should have an acceptable value of Li-ion conductivity, low electronic conductivity and chemical stability with metallic Li.[22–24] The Li-ion conductivity ensures effective ionic transport across the SSE/Li interface, and the electronic insulation prevents undesirable side reactions between the SSEs and Li metal anodes.

Lithium phosphorus oxynitride (LiPON) is an amorphous SSE which has been reported to completely prevent Li dendrite penetration from the anode to cathode under low current density in thin-film batteries.[27] The most important feature of these LiPON thin-films is that they can be prepared to be homogeneous, without either grain boundaries or porosity.[28] Sputtered LiPON thin-films that are both amorphous and uniform are stable in contact with Li metal, and form an Li-ion conductive ($\sim 1$ μS cm$^{-1}$) but almost electronically insulating ($\sim 10^{14}$ Ω cm) interlayer.[29,30] Homogenous sputtered LiPON thin-films used as an SSE have resulted in uniform Li plating/stripping over 10 000 cycles in thin-film batteries with lithium nickel manganese oxide cathodes and Li metal anodes.[31] With these superior chemical and electrochemical stabilities, the use of LiPON thin-films on bulk SSEs seems a promising way to form stable and ionically conductive interlayers between fast Li-ion conducting SSEs and Li metal.[29]

Here we report the growth of thin interlayers of LiPON between argyrodite $Li_6PS_5Cl$ SSEs and Li metal anodes *via* radio frequency (RF) sputtering. The LiPON thin interlayers show an ionic conductivity of 0.69 and 0.98 μS cm$^{-1}$ for Li-ion conductivity at 25 and 30 °C, respectively, which is beneficial for rapid Li-ion transport across the interface between SSEs and Li metal. The $Li_6PS_5Cl$ SSEs with LiPON interlayers also show a superior wetting interaction with heated Li metal, consequently reducing the interfacial resistance to as low as 1.3 Ω cm$^2$. Li/LiPON/$Li_6PS_5Cl$/LiPON/Li symmetric cells reached a high critical current density value of 4.1 mA cm$^{-2}$, and stable cycling for over 1000 h at 0.5 mA cm$^{-2}$ at 30 °C. This excellent performance of Li/LiPON/$Li_6PS_5Cl$/LiPON/Li symmetric cells can be attributed to homogenous Li plating/stripping encouraged by the LiPON interlayers. These results demonstrate an encouraging design for improved wetting, ionic conductivity and stability of the interfaces between argyrodite SSEs and Li metal anodes, and a promising strategy to improve the performance of solid-state Li metal batteries.

The SEM image in Fig. 1a is from the top surface of a sintered $Li_6PS_5Cl$ SSE, and exhibits the rather loose packing of micrometer-sized grains of this material.[32] The upper-right inset of Fig. 1a is a digital image of a grey–white argyrodite $Li_6PS_5Cl$ ceramic pellet with 1 mm thickness. The FIB-SEM cross-section image in Fig. 1b shows the porosity surrounding the individual grains inside these bulk $Li_6PS_5Cl$ pellets. Most of the grains are larger than 5 μm, and the density of these sintered pellets was estimated to be 93% of the theoretical value. EIS was performed to measure the Li-ion conductivity of these sintered $Li_6PS_5Cl$ pellets with two Pt electrodes, and typical EIS curves collected over the temperature range from 25 to 50 °C are shown in the Nyquist plot in Fig. 1c. The semicircles at high frequencies correspond to the combined bulk and grain boundary response, and the low frequency spikes are attributed to the capacitive behaviour of the Pt blocking electrodes. The Li-ion conductivity was calculated to be 6.7 and 8.3 mS cm$^{-1}$ at 25 and 30 °C, respectively, and increases systematically with temperature from 25 to 50 °C. The Arrhenius behaviour for the resulting Li-ion conductivities is plotted in Fig. 1d, and an activation energy of 0.37 eV was calculated using the Arrhenius equation, a similar value that measured by other workers.[33]

To understand the morphology of LiPON layer at the interface between $Li_6PS_5Cl$ SSEs and Li metal anodes, a series of characterization techniques were used. Fig. 2a and b exhibit top-view SEM images of bare and LiPON coated $Li_6PS_5Cl$ pellet surfaces, respectively. As shown in Fig. 2b, the edges of the $Li_6PS_5Cl$ grains appear obviously smoother on the LiPON-coated surface, demonstrating a dense covering by the sputtered LiPON thin film. The colour of the argyrodite $Li_6PS_5Cl$ pellet also changed from grey-white to brown-yellow after the LiPON coating, as shown in the digital image insets in Fig. 2a and b. EDX mapping images were obtained on the surfaces of bare and LiPON-coated $Li_6PS_5Cl$ pellets, as shown in Fig. S2 (ESI†). From Fig. S2a0-5 (ESI†), neither O nor N signals can be detected from the bare $Li_6PS_5Cl$ pellet, while P, O, and N are all

 

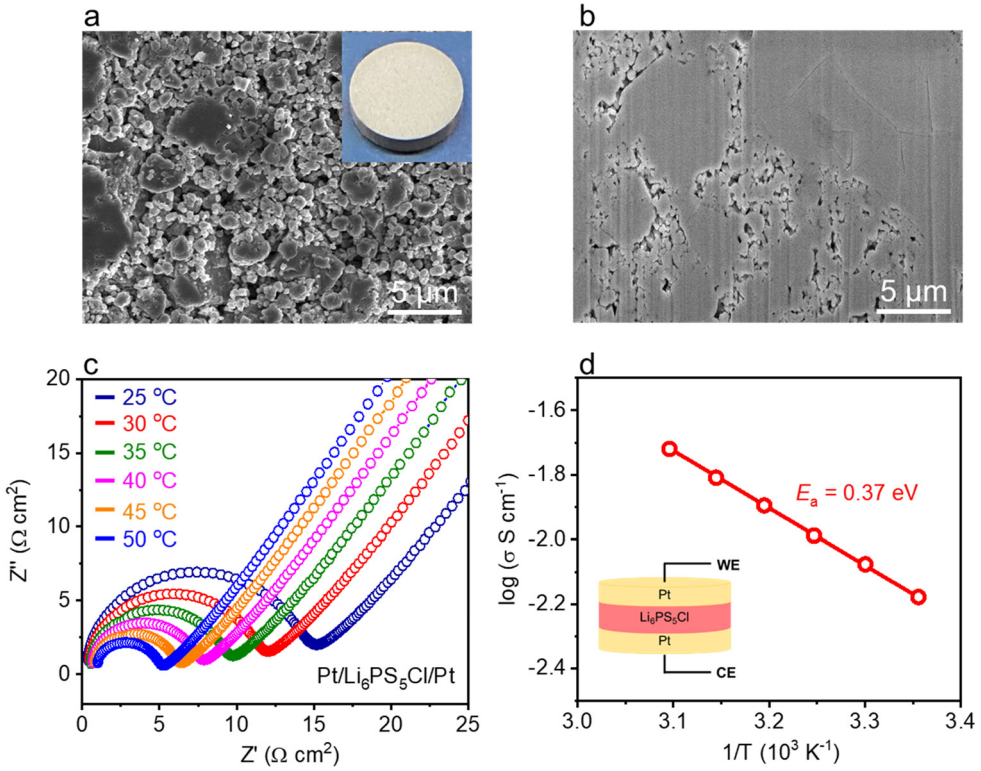


Fig. 1 (a) Top-view SEM image of the surface morphology of a sintered $Li_6PS_5Cl$ ceramic pellet. The upper-right inset is a digital photo of the $Li_6PS_5Cl$ pellet. (b) FIB-SEM cross-sectional image of the sintered $Li_6PS_5Cl$ pellet. (c) EIS curves of a Pt/$Li_6PS_5Cl$/Pt symmetric cell measured at temperatures from 25–50 °C with (d) the corresponding Arrhenius plot of the $Li_6PS_5Cl$ ionic conductivity.

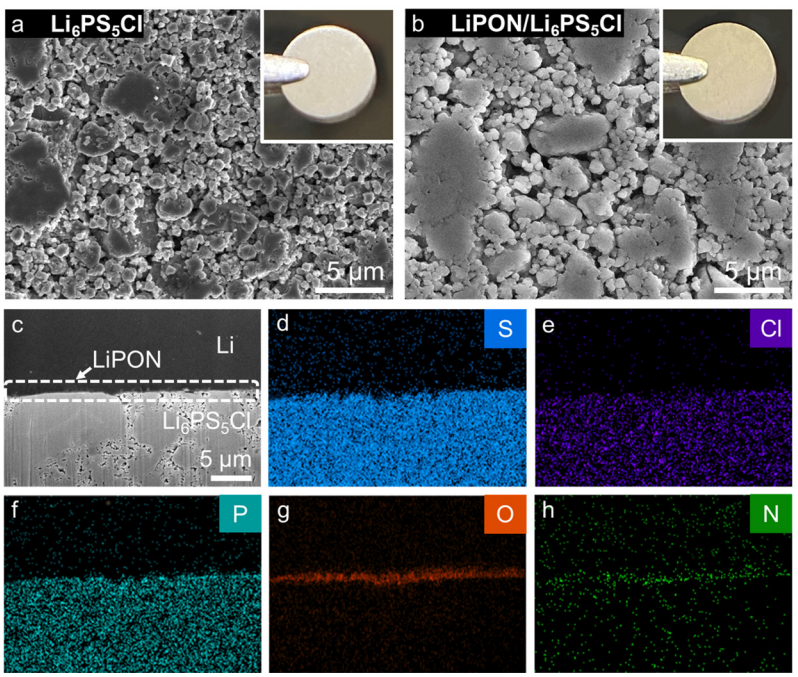


Fig. 2 Top-view SEM images of the surface morphologies of the $Li_6PS_5Cl$ pellet (a) without and (b) with LiPON coating. The upper-right insets are digital photos of the bare $Li_6PS_5Cl$ and LiPON coated $Li_6PS_5Cl$ pellets. (c) FIB-SEM cross-sectional image of the LiPON coated $Li_6PS_5Cl$ SSE and Li metal interface, with (d–h) corresponding EDX mapping images for S, Cl, P, O, and N.

uniformly distributed over the entire surface area in the coated sample (Fig. S2b0-5, ESI†), further demonstrating the homogeneous coating of LiPON on the surface of the $Li_6PS_5Cl$ pellet. EDX mapping was also performed on a cross-section of

the LiPON coated $Li_6PS_5Cl$ SSE/Li metal interface, as shown in Fig. 2c–h. The O and N are distributed uniformly at the interface between the $Li_6PS_5Cl$ SSE and Li metal electrodes, indicating a homogeneous thin LiPON interlayer has been deposited.

To investigate the surface compositions, crystallinity and phase purity of the $Li_6PS_5Cl$ SSE, and the effects of interfacial modification, XPS, FTIR and XRD analysis was conducted on the surfaces of bare and LiPON-coated $Li_6PS_5Cl$ pellets. The XPS peaks at binding energies of 54, 133, 160 and 198 eV from the bare $Li_6PS_5Cl$ pellet were assigned to Li 1s, P 2p, S 2p, and Cl 2p excitations, respectively, as shown in Fig. 3a. In the XPS spectrum from the LiPON-coated $Li_6PS_5Cl$ pellet, the observation of P 2p and O 1s peaks with increased intensities at binding energies of 133 and 532 eV, and S 2p, Cl 2p, S 2s and Cl 2s excitation peaks with decreased intensities at binding energies of 160, 198, 225, and 269 eV, as well as the appearance of the N 1s peak at 397 eV, confirmed the presence of LiPON. XPS peaks for P 2p, N 1s, and O 1s regions from the surface of LiPON coated $Li_6PS_5Cl$ SSEs are shown in Fig. S3 (ESI†), and match well with those reported to identify the chemical characteristics of LiPON.[34] The FTIR spectra in Fig. 3b and Fig. S4a (ESI†) from the bare $Li_6PS_5Cl$ SSE showed a strong peak at

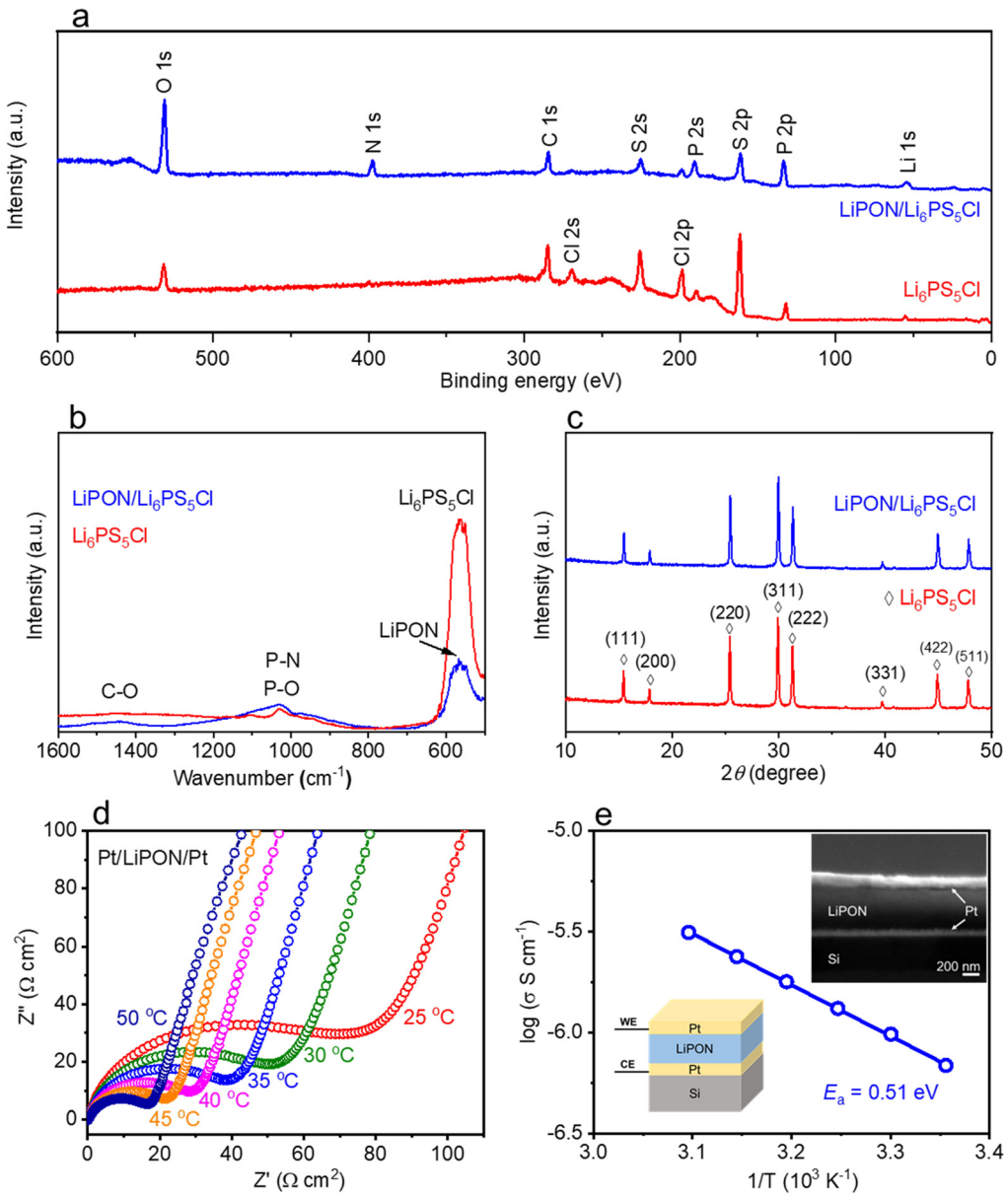


Fig. 3 (a) XPS spectra from $Li_6PS_5Cl$ SSEs with and without LiPON thin-film coating. The peak at the binding energy of 284.8 eV was assigned to the C 1s excitations on both surfaces of bare and LiPON coated $Li_6PS_5Cl$ pellets, possibly because of the weak ambient contamination during sample transfer to the characterization equipment. (b) XRD patterns and (c) FTIR spectra of $Li_6PS_5Cl$ SSEs with and without LiPON thin-film interlayers. ◊ corresponds to peaks from the cubic argyrodite $Li_6PS_5Cl$ phase. (d) EIS curves of a Pt/LiPON/Pt symmetric cell at temperatures from 25–50 °C with (e) the corresponding Arrhenius plot of the LiPON ionic conductivity. The bottom-left inset is a schematic illustration of the Pt/LiPON/Pt symmetric cell structure with the corresponding SEM cross-sectional image (upper-right inset).

 

560 $cm^{-1}$ consistent with the formation of the argyrodite $Li_6PS_5Cl$ phase, and the peak at the same wavenumber with decreased intensity after LiPON coating indicated a dense LiPON covering the surface of the $Li_6PS_5Cl$ SSE. The broad and weak C–O stretching peaks at ~1500 $cm^{-1}$ and the absence of other peaks related to impurities demonstrate only slight ambient contamination on the surface of these $Li_6PS_5Cl$ pellets. As shown in Fig. 3c, all the diffraction peaks obtained on both the bare and LiPON-coated $Li_6PS_5Cl$ pellets can be attributed to the cubic argyrodite phase ($F\bar{4}3m$ space group) without any impurity phases. The LiPON thin film coating did not significantly affect the observation of the diffracted peaks from the $Li_6PS_5Cl$ SSE because it was amorphous (as confirmed and shown in Fig. S4b, ESI†) and only 30 nm thick.

To characterize the electrochemical properties of the thin LiPON coating layer, EIS was performed on samples of a thicker sputtered LiPON thin-film with two Pt electrodes. The EIS profiles collected from the Pt/LiPON/Pt symmetric cell from 25 to 50 °C are shown in Fig. 3d. The bottom-left and upper-right insets in Fig. 3e are a schematic illustration and cross-sectional SEM view of the Pt/LiPON/Pt symmetric cell. The resulting Nyquist plots exhibit semicircular features indicating typical ion conducting behaviour, and the Li-ion conductivity of the amorphous LiPON thin film was calculated to be 0.69 and 0.98 μS $cm^{-1}$ at 25 and 30 °C, respectively, and increases with temperature from 25 to 50 °C. The corresponding Arrhenius behaviour is plotted in Fig. 3e, and the calculated activation energy was 0.51 eV in good agreement with the literature values for LiPON thin films.[30] EDX mapping on the cross-section of a LiPON/Si sample prepared by the PVD system in the glovebox is shown in Fig. S5 (ESI†). The P, O and N signals are distributed uniformly through the LiPON thin-film. From this analysis, we concluded that these sputtered LiPON thin films are continuous, amorphous and have ionic conductivities well suited for modifying the interfaces between SSEs and Li metal anodes in SSBs.

Over the range of LiPON film thicknesses tested, the 30 nm interlayers offered the best combination of low interface resistance and long-term stability (Fig. S6, ESI†). To explore the effect of LiPON interlayers on the contact between the $L_6PS_5Cl$ SSE and Li metal, interfacial modification was carried out by depositing a 30 nm thick LiPON layer on the surface of the $Li_6PS_5Cl$ pellet using RF sputtering. A Li metal disk electrode of 60 μm thickness was pressed onto the surface of this LiPON coated $Li_6PS_5Cl$ pellet, and the resulting Li and LiPON stack on the $Li_6PS_5Cl$ pellet was heated at 80 °C under a pressure of 2.3 MPa for 12 h to achieve a conformal contact. A control sample was prepared using a bare $Li_6PS_5Cl$ pellet by the same process. Fig. 4a shows a schematic of the loose interfacial contact between the bare $Li_6PS_5Cl$ SSE and Li metal electrode, and a corresponding FIB-SEM cross-section image in Fig. 4b of the interface between $Li_6PS_5Cl$ SSE and Li metal with an almost continuous micron-sized gap, indicating that the $Li_6PS_5Cl$ SSE without LiPON coating makes poor interfacial contact with the Li metal electrode even under pressure and heating. A cross-sectional SEM image of the interface between bare $Li_6PS_5Cl$ SSE

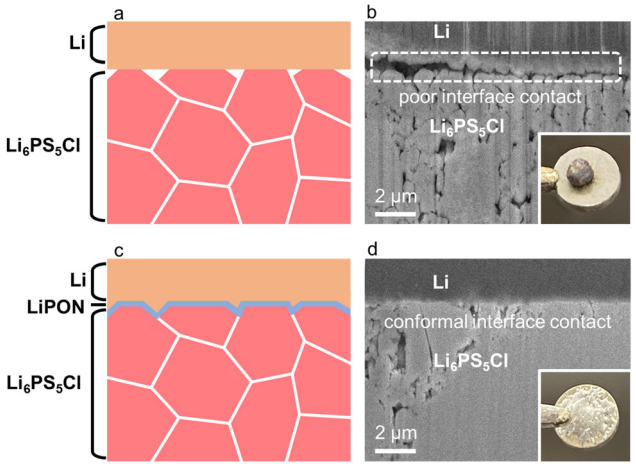


Fig. 4 (a) Schematic of a poor interfacial contact between $Li_6PS_5Cl$ SSE and a Li metal electrode. (b) FIB-SEM cross-section image of the interface between the un-coated $Li_6PS_5Cl$ SSE and Li metal. The $Li_6PS_5Cl$ SSE without a LiPON coating has poor interfacial contact with the Li metal electrode. The bottom-right inset is the digital photo of a droplet of molten Li forming a ball on the surface of the $Li_6PS_5Cl$ pellet. (c) Schematic of the improved wetting behaviour of a coated $Li_6PS_5Cl$ SSE with the Li metal anode. (d) FIB-SEM cross-section image of the interface between the LiPON coated $Li_6PS_5Cl$ SSE and Li metal. The Li metal is in good contact with the LiPON-coated $Li_6PS_5Cl$ SSE over the whole imaged area. The bottom-right inset is the digital photo of superior wetting behaviour of liquid Li on the LiPON-coated $Li_6PS_5Cl$ SSE.

and Li metal revealed by breaking the $Li_6PS_5Cl$ pellet, in Fig. S7a (ESI†), also exhibits interfacial voids between the $Li_6PS_5Cl$ SSE and Li metal. It is important to compare the FIB-milled and fractured cross-sections to be confident that any local heating arising from the FIB-milling process does not modify the interfacial wetting behaviour. Fig. 4c is a schematic of the improved wetting behaviour of $Li_6PS_5Cl$ SSE by introducing a LiPON interlayer, and the corresponding FIB-SEM cross-section image of the same interface is shown in Fig. 4d. This demonstrates that the thin LiPON interlayer helps the Li metal to contact conformally with the surface of $Li_6PS_5Cl$ SSE during the pressing and heating step, essentially removing all the interfacial voids. The bottom-right insets in Fig. 4b and Fig. S7a (ESI†) are digital photos of a droplet of molten Li formed a ball on the surface of the bare $Li_6PS_5Cl$ pellet, demonstrating poor wetting of the bare $Li_6PS_5Cl$ SSE. The bottom-right insets of Fig. 4d and Fig. S7b (ESI†) are digital photos of molten Li spreading out uniformly over the surface of the LiPON coated $Li_6PS_5Cl$ pellet, demonstrating the improved wetting behaviour of the coated $Li_6PS_5Cl$ SSE. This lack of interfacial voids is confirmed in the cross-sectional SEM image of the interface in a LiPON coated $Li_6PS_5Cl$ pellet sample in Fig. S7b (ESI†). The series milling slices of FIB-SEM cross-sections of the interfaces between the $Li_6PS_5Cl$ SSE and Li metal without and with the LiPON coating also show in 3D the void-free interface morphology between the LiPON-coated $Li_6PS_5Cl$ SSE and Li metal, as shown in Fig. S8a and b (ESI†), further demonstrating that the improved interfacial contact spreads across the entire interface. EIS profiles of LiPON coated

symmetric cells with Pt electrodes (Pt/LiPON/$Li_6PS_5Cl$/LiPON/Pt) were measured from 25 to 50 °C, as shown in Fig. S9a (ESI†). The resulting Nyquist plots exhibit semicircular features, and the ionic conductivity of the LiPON coated symmetric cell was calculated to be 5.9 and 7.6 mS $cm^{-1}$ at 25 and 30 °C, respectively, and increases with temperature from 25 to 50 °C. The corresponding Arrhenius behaviour is plotted in Fig. S9b (ESI†), and the calculated activation energy was 0.41 eV. The ionic conductivity at 30 °C of the LiPON coated symmetric cell, 7.6 mS $cm^{-1}$, is slightly lower than that measured on the bare symmetric cell (Pt/$Li_6PS_5Cl$/Pt), 8.3 mS $cm^{-1}$, which shows that the LiPON interlayer does marginally affect Li-ion transfer across the interface at this temperature. However, a much more beneficial effect of the LiPON interlayer is that it significantly improved the wettability of $Li_6PS_5Cl$ SSE, which provides conformally interfacial contact with the Li anode.

The critical current density is a pivotal parameter to evaluate the stability of the interface between the $Li_6PS_5Cl$ SSE and Li anode, and to demonstrate the efficiency by which Li dendrite growth can be suppressed. For these critical current density measurements at 30 °C the applied current density was increased from 0.1 mA $cm^{-2}$ with a step increase of 0.1 mA $cm^{-2}$ until cell failure, with the capacity of each Li plating/stripping step being 0.5 mA h $cm^{-2}$ (corresponding to the transfer of approximately 2.5 μm thick Li metal). The critical current density was defined as the current density at which a sharp drop in voltage was observed (cell failure). The potential profiles of the Li/$Li_6PS_5Cl$/Li and Li/LiPON/$Li_6PS_5Cl$/LiPON/Li symmetric cells undergoing this critical current density measurement are shown in Fig. 5a and b, respectively. The bottom-left insets are a schematic illustration of the symmetric cell structures. The critical current density of the Li/$Li_6PS_5Cl$/Li symmetric cell was 1.0 mA $cm^{-2}$, while the critical current density of the Li/LiPON/$Li_6PS_5Cl$/LiPON/Li symmetric cell was significantly improved to 2.7 mA $cm^{-2}$ (as shown in magnified details in Fig. 5c). This is consistent with the improved conformal interfacial contact between the LiPON-coated $Li_6PS_5Cl$ SSE and Li metal, as shown in the SEM images in Fig. 4b and d.

EIS profiles were obtained at different stages of the critical current density measurements on a Li/LiPON/$Li_6PS_5Cl$/LiPON/Li symmetric cell; on a fresh cell before applying a current, after applying a current density of 2.0 mA $cm^{-2}$, and after sudden drop in voltage (short circuit), as shown in Fig. S10 (ESI†). The total resistance (sum of the bulk and grain boundary resistance of the SSE and the SSE/Li interfacial resistance) was measured. The total resistance values before cycling and after applying a current density of 2.0 mA $cm^{-2}$ were almost unchanged at ~15 Ω $cm^2$, indicating that the Li/LiPON/$Li_6PS_5Cl$/LiPON/Li symmetric cell has interfaces that remain electrochemically stable during Li plating/striping cycling at least up to this current density. The EIS spectrum obtained before cycling shows, as expected, a semicircular feature corresponding to an ionic conductor, but after the sudden drop in voltage a clear short circuit between the two Li electrodes was measured possibly because of formation of Li dendrites that penetrate the $Li_6PS_5Cl$ pellet. To confirm this dendrite growth, we disassembled the short-circuited Li/$Li_6PS_5Cl$/Li symmetric cell, and carried out FIB-SEM on the surface and a cross-section of the disassembled $Li_6PS_5Cl$ SEE to observe the morphological details of any dendrite formation. Top-view SEM images of Li dendrite growth inside the surface of the $Li_6PS_5Cl$ SSE after short-circuiting at 1.0 mA $cm^{-2}$ in the Li/$Li_6PS_5Cl$/Li symmetric cell are shown in Fig. S11a–f (ESI†), and FIB-SEM cross-sectional images of Li dendrite growth inside the surface area and propagation into the bulk of the $Li_6PS_5Cl$ SSE are shown in Fig. S11g–l (ESI†). Although these FIB-SEM images do not show the Li dendrite penetrating the entire electrolyte and shorting between the two electrodes, we have obtained SEM images of Li dendrites ~150 μm in width at the surface and propagating ~10 μm into the bulk. We believe that these observations are at least suggestive that isolated lithium dendrites have grown through the entire $Li_6PS_5Cl$ SSE and contacted the two Li metal electrodes, resulting in short-circuiting at 1.0 mA $cm^{-2}$ of the Li/$Li_6PS_5Cl$/Li symmetric cell. In contrast, when the Li/LiPON/$Li_6PS_5Cl$/LiPON/Li symmetric cell carried a current density of 1 mA $cm^{-2}$, the corresponding voltage was relatively stable, which indicates that dendrite growth is suppressed by the introduced the LiPON interlayer. From Fig. S12 (ESI†) the O and N signals are still distributed uniformly at the interface between the $Li_6PS_5Cl$ SSE and Li metal electrodes after the cell failure, indicating the thin LiPON interlayer retained its integrity after multiple cycles of Li plating and stripping in the critical current density measurements.

Because of the dramatically enhanced wetting behaviour at the LiPON-coated $Li_6PS_5Cl$ SSE/Li metal interface, we expect the interfacial resistance between LiPON-coated $Li_6PS_5Cl$ SSE and Li metal might be reduced. We have compared the interfacial resistances in Li/$Li_6PS_5Cl$/Li and Li/LiPON/$Li_6PS_5Cl$/LiOPN/Li symmetric cells before the critical current density measurements were started (corresponding to symmetric cells shown in Fig. 5a and b), as well as measuring the performance of the Pt/$Li_6PS_5Cl$/Pt symmetric cell under 30 °C in Fig. 1c. As shown in Fig. 5d, the Nyquist plots of the Li/$Li_6PS_5Cl$/Li, Li/LiPON/$Li_6PS_5Cl$/LiPON/Li and Pt/$Li_6PS_5Cl$/Pt symmetric cells exhibit high frequency semicircles and low-frequency tails. The semicircles at high frequencies correspond to the total resistance of bulk and grain boundaries in the SSE, while the semicircle or tails at low frequencies are attributed to both capacitive and resistive behaviour of the Li metal electrodes but only the capacitive behaviour of the blocking Pt electrodes. The total resistance of the $Li_6PS_5Cl$ SSE in the Pt/$Li_6PS_5Cl$/Pt symmetric cell is 12.0 Ω $cm^2$, lower than achieved in either symmetric cell with Li metal electrodes. The Li/$Li_6PS_5Cl$/Li symmetric cell shows a total resistance of 20.6 Ω $cm^2$, which consists of the sum of the total resistance (bulk and grain boundary) of the $Li_6PS_5Cl$ SSE and the interfacial resistance of the bare $Li_6PS_5Cl$ SSE/Li metal electrode. The interfacial resistance between bare $Li_6PS_5Cl$ SSE and Li metal can then be estimated as 4.3 Ω $cm^2$ because two interfaces between $Li_6PS_5Cl$ SSE and Li metal are present in each Li/$Li_6PS_5Cl$/Li symmetric cell. In a similar way, using a measured overall resistance of 14.7 Ω $cm^2$ for the Li/LiPON/$Li_6PS_5Cl$/LiPON/Li symmetric cell allows us to estimate

 

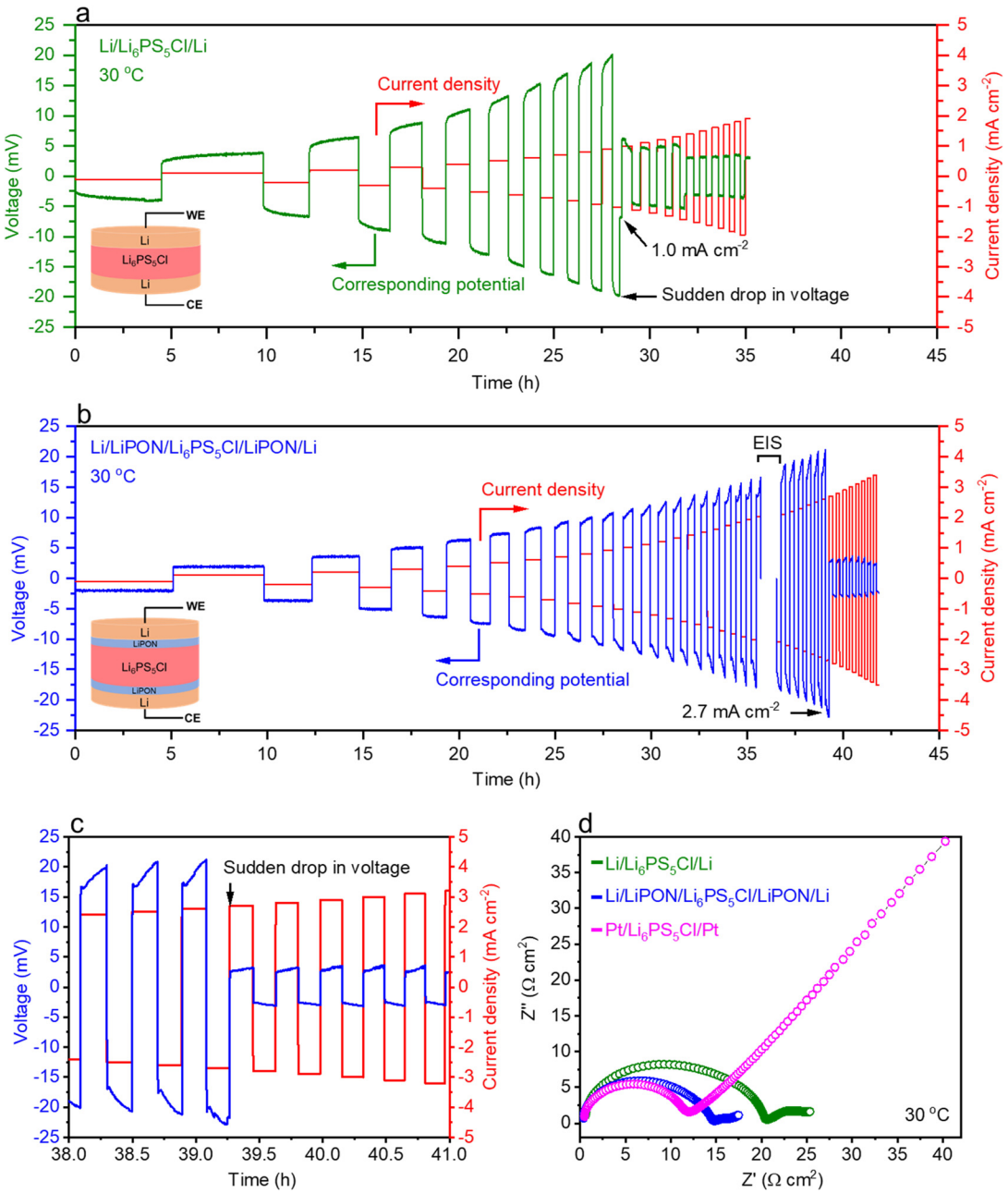


Fig. 5 Potential response of (a) $Li/Li_6PS_5Cl/Li$ and (b) $Li/LiPON/Li_6PS_5Cl/LiPON/Li$ symmetric cells undergoing a critical current density measurement at 30 °C. The bottom-left insets are a schematic illustration of the symmetric cell structures. (c) Magnified potential response near the critical current density of the $Li/LiPON/Li_6PS_5Cl/LiPON/Li$ symmetric cell. The drastic voltage drop corresponds to short-circuiting (cell failure). (d) Comparison of EIS profiles of the $Li/Li_6PS_5Cl/Li$, $Li/LiPON/Li_6PS_5Cl/LiPON/Li$ and $Pt/Li_6PS_5Cl/Pt$ symmetric cells at 30 °C.

the resistance of one interface between the LiPON-coated $Li_6PS_5Cl$ SSE and Li metal to be 1.3 Ω $cm^2$, much lower than that in the bare $Li_6PS_5Cl$ SSE based symmetric cells. Therefore, it does seem that the improved wetting behaviour achieved by adding a thin LiPON interlayer does contribute to a significantly reduced interfacial resistance, and presumably encourages efficient Li-ion exchange between the $Li_6PS_5Cl$ SSE and Li metal electrodes.

We have discussed above that the current density measurements suggest that the interface between SSE and Li metal is stabilised by addition of a thin LiPON layer, and that this results in significant improvements in critical current density in Li metal electrodes based symmetric cells. However, cell failure is still observed at high current densities, so it is important to understand the local Li mass transfer processes at the interface between the SSE and Li metal at high polarizations which may give rise to inhomogeneous current densities and facilitate dendrite growth.[35] A relaxation step (without applied current) after each Li plating and stripping cycle can help equilibrate the Li concentration in the bulk of the SSE, and

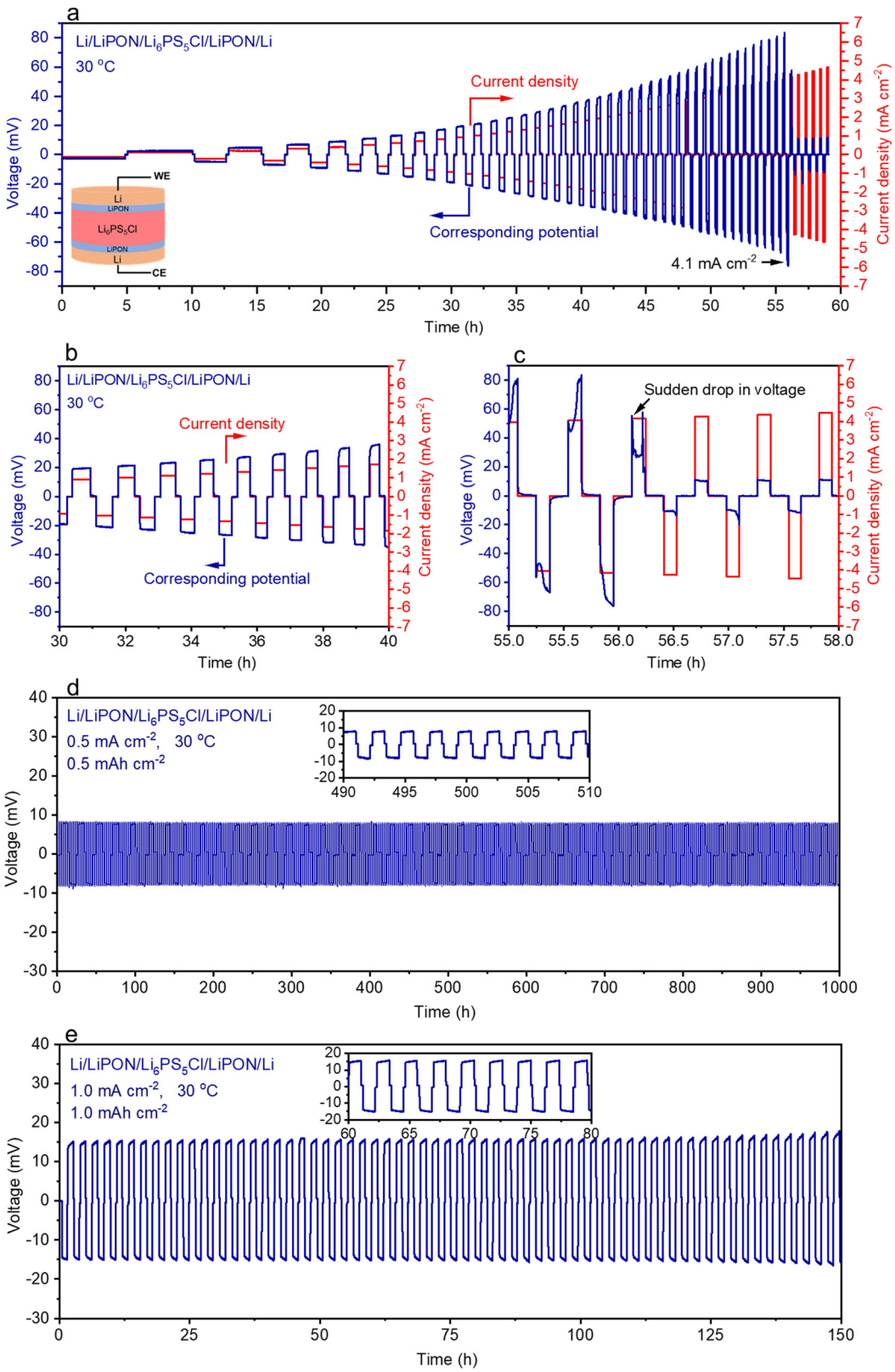


Fig. 6 Potential response of (a) Li/LiPON/$Li_6PS_5Cl$/LiPON/Li symmetric cell undergoing a critical current density measurement with a relaxation process at 30 °C. The bottom-left insets are a schematic illustration of the symmetric cell structures. (b) Expanded potential response of the cell over the time range from 30 to 40 h, and (c) near the sudden drop in voltage corresponding to cell failure. (d) and (e) Galvanostatic cycling performance for 1 h in each half cycle of the Li/LiPON/$Li_6PS_5Cl$/LiPON/Li symmetric cell under applied current densities of 0.5 mA $cm^{-2}$ and 1.0 mA $cm^{-2}$ at 30 °C, respectively.

 

plays an important role in encouraging efficient Li mass transport in the next cycle.[36] To study the effect of relaxation processes on the cells, we carried out critical current density measurements on Li/LiPON/$Li_6PS_5Cl$/LiPON/Li symmetric cells by adding a relaxation step for 10 minutes after each half cycle. As before, the applied current densities were increased from 0.1 mA $cm^{-2}$ with an increase of 0.1 mA $cm^{-2}$ after each step of Li plating/stripping capacity of 0.5 mA h $cm^{-2}$ at 30 °C until the cell short-circuited, and the potential profiles are shown in Fig. 6a–c. Compared with the critical current density measurements without the relaxation process (shown in Fig. 5b), the critical current density was significantly improved from 2.7 to 4.1 mA $cm^{-2}$ (as shown in the magnified details in Fig. 6c), and the corresponding maximum polarization voltage was increased from ~20 mV to ~80 mV. Unlike the rapidly increased polarization voltage shown in Fig. 5b, the potential profile obtained with the relaxation process remained smooth and stable around a current density of 2 mA $cm^{-2}$ for the Li/LiPON/$Li_6PS_5Cl$/LiPON/Li symmetric cell, as shown in Fig. 6b, indicating rather uniform and stable Li plating/stripping at interface between the SSE and Li metal. Therefore, it can be concluded that this simple relaxation process can improve the uniformity of Li mass transport in subsequent cycles, consequently stabilise the voltage polarization effect and achieve higher values of critical current density in Li/LiPON/$Li_6PS_5Cl$/LiPON/Li symmetric cells. We believe that this critical current density of 4.1 mA $cm^{-2}$ is the highest value obtained for argyrodite $Li_6PS_5Cl$ SSE around room temperature (as shown by the summary of results from the literature shown in Table S1, ESI†).

Based on this demonstration of the advantage of the relaxation process, we further applied galvanostatic Li plating/stripping experiments to evaluate the long-term interfacial stability and Li-ion migration capability at the interface between the $Li_6PS_5Cl$ SSE and Li metal at 30 °C. As shown in Fig. 6d, the Li/LiPON/$Li_6PS_5Cl$/LiPON/Li symmetric cell maintained stable cycling for 1000 h with a stabilized polarization voltage of 7.9 mV at a current density of 0.5 mA $cm^{-2}$ (capacity of 0.5 mA h $cm^{-2}$), and the calculated total resistance of 15.8 Ω $cm^2$ was maintained stably during cycling and is good agreement with the resistance (14.7 Ω $cm^2$) measured by EIS (Fig. 5d). It should be mentioned that the stable performance of these cells is strongly influenced by the enhanced interface wetting achieved by introducing the LiPON interlayer to give improved conformal interfacial contact. We suggest that it is the combination of the amorphous nature and reasonable ionic conductivity of the LiPON interlayer that plays an important role in stabilizing the interface between the SSE and Li metal, the first because it gives some flexibility when the Li metal is brought into contact with a thin and stable oxynitride layer and the second because it results in low interfacial impedance. The interfacial resistance value was estimated to be 1.9 Ω $cm^2$, making a contribution of only 1.9 mV to the total voltage of the symmetric cell at applied current density of 0.5 mA $cm^{-2}$. Additionally, Li/LiPON/$Li_6PS_5Cl$/LiPON/Li symmetric cells were able to maintain stability over hundreds of hours even with a higher capacity of 1.0 mA h $cm^{-2}$ at a current density of 1.0 mA $cm^{-2}$, as shown in Fig. 6e. In contrast, the galvanostatic cycling of a symmetric cell without the LiPON thin-film coating showed a noisy potential profile with large voltage polarization at applied current density of 0.5 mA $cm^{-2}$ (as shown in Fig. S13, ESI†), demonstrating non-uniform Li plating/stripping at the interface between the SSE and Li metal. It concludes from these measurements that the interfacial resistance has a major impact on the Li plating/stripping at the interface between the SSE and Li metal, and that the high interfacial resistance between the bare $Li_6PS_5Cl$ SSE and Li metal contributes to non-uniform current densities across the interface, causing further short-circuiting. The improved conformal interfacial contact by introducing a thin LiPON interlayer is able to reduce the interfacial impedance and the Li-ion conducting LiPON interlayer provides pathways for efficient Li-ion migration, both of which encourage homogenous Li plating/stripping at the interface. Therefore, the LiPON thin-film coating significantly improves the interfacial contact and stabilized the interface between SSEs and Li metal anodes, and has great potential to overcome some of the primary challenges for the practical application of solid-state Li metal batteries.

## Conclusions

We have demonstrated a strategy to improve the interfacial contact and stabilize the interface between $Li_6PS_5Cl$ and Li metal anodes by introducing a thin amorphous LiPON interlayer. The dramatically enhanced wetting behaviour of the $Li_6PS_5Cl$ SSE provides a conformally interfacial contact with Li metal. We suggest that the thin LiPON interlayer has a higher ionic conductivity than that of the interphase layer formed between argyrodite SSE and Li metal, facilitating Li-ion migration across the interface, and the electronically insulating property of the LiPON interlayers also helps to suppress these side reactions. The glassy nature of the amorphous LiPON interlayer may improve the mechanical contact between SSEs and Li metal because it will have some degree of flexibility, as demonstrated by the interlayer surviving after. LiPON coated $Li_6PS_5Cl$ symmetric cells exhibit a reduction in interfacial resistance to as low as 1.3 Ω $cm^2$ and show stable Li plating/striping cycling over 1000 h with stabilized polarization voltage of 7.9 mV under 0.5 mA $cm^{-2}$. The critical current density of LiPON coated $Li_6PS_5Cl$ symmetric cells reached a high value of 4.1 mA $cm^{-2}$ at 30 °C. We believe that our strategy to overcome the interface contact issue and stabilize the interface between the argyrodite SSE and Li metal could be applied to other types of SSEs, and also be extended to all solid-state batteries using Li metal as the anode.

## Author contributions

J. S. contributed to all aspects of the research. C. R. M. G. supervised the project. J. S. prepared pellets and cells, and conducted all physical characterizations and electrochemical

experiments. J. S., Z. N., and X. G. discussed processes of pellets and pouch cells preparation. J. S., M. P., and C. R. M. G. discussed the data. J. S. and C. R. M. G. wrote the manuscript with contributions from all authors.

## Conflicts of interest

There are no conflicts to declare.

## Acknowledgements

The authors acknowledge the financial support of the Faraday Institution (SOLBAT project, FIRG007). The authors also grateful thank the David Cockayne Centre for Electron Microscopy, Department of Materials, University of Oxford.

## References

1 M. Armand and J. M. Tarascon, *Nature*, 2008, **451**, 652–657.
2 W. Xu, J. L. Wang, F. Ding, X. L. Chen, E. Nasybutin, Y. H. Zhang and J. G. Zhang, *Energy Environ. Sci.*, 2014, **7**, 513–537.
3 R. W. Mo, X. Y. Tan, F. Li, R. Tao, J. H. Xu, D. J. Kong, Z. Y. Wang, B. Xu, X. Wang, C. M. Wang, J. L. Li, Y. T. Peng and Y. F. Lu, *Nat. Commun.*, 2020, **11**, 1374.
4 M. R. Palacin and A. de Guibert, *Science*, 2016, **351**, 6273.
5 H. J. Chang, A. J. Ilott, N. M. Trease, M. Mohammadi, A. Jerschow and C. P. Grey, *J. Am. Chem. Soc.*, 2015, **137**, 15209–15216.
6 J. E. Ni, E. D. Case, J. S. Sakamoto, E. Rangasamy and J. B. Wolfenstine, *J. Mater. Sci.*, 2012, **47**, 7978–7985.
7 J. Su, T. Tsuruoka, T. Tsujita, Y. Nishitani, K. Nakura and K. Terabe, *Chem. Mater.*, 2019, **31**, 5566–5575.
8 Y. G. Lee, S. Fujiki, C. H. Jung, N. Suzuki, N. Yashiro, R. Omoda, D. S. Ko, T. Shiratsuchi, T. Sugimoto, S. Ryu, J. H. Ku, T. Watanabe, Y. Park, Y. Aihara, D. Im and I. T. Han, *Nat. Energy*, 2020, **5**, 348.
9 J. Janek and W. G. Zeier, *Nat. Energy*, 2016, **1**, 16141.
10 J. Su, T. Hisatomi, T. Minegishi and K. Domen, *Angew. Chem., Int. Ed.*, 2020, **59**, 13800–13806.
11 S. Chu and A. Majumdar, *Nature*, 2012, **488**, 294–303.
12 W. D. Richards, L. J. Miara, Y. Wang, J. C. Kim and G. Ceder, *Chem. Mater.*, 2016, **28**, 266–273.
13 Z. Z. Zhang and L. F. Nazar, *Nat. Rev. Mater.*, 2022, **7**, 389–405.
14 R. Murugan, V. Thangadurai and W. Weppner, *Angew. Chem., Int. Ed.*, 2007, **46**, 7778–7781.
15 J. F. Ihlefeld, P. G. Clem, B. L. Doyle, P. G. Kotula, K. R. Fenton and C. A. Apblett, *Adv. Mater.*, 2011, **23**, 5663–5667.
16 G. F. Ortiz, M. C. Lopez, P. Lavela, C. Vidal-Abarca and J. L. Tirado, *Solid State Ionics*, 2014, **262**, 573–577.
17 C. Yu, L. van Eijck, S. Ganapathy and M. Wagemaker, *Electrochim. Acta*, 2016, **215**, 93–99.
18 S. Boulineau, M. Courty, J. M. Tarascon and V. Viallet, *Solid State Ionics*, 2012, **221**, 1–5.
19 D. H. S. Tan, E. A. Wu, H. Nguyen, Z. Chen, M. A. T. Marple, J. M. Doux, X. F. Wang, H. D. Yang, A. Banerjee and Y. S. Meng, *ACS Energy Lett.*, 2019, **4**, 2418–2427.
20 W. Luo, Y. H. Gong, Y. Z. Zhu, K. K. Fu, J. Q. Dai, S. D. Lacey, C. W. Wang, B. Y. Liu, X. G. Han, Y. F. Mo, E. D. Wachsman and L. B. Hu, *J. Am. Chem. Soc.*, 2016, **138**, 12258–12262.
21 W. Luo, Y. H. Gong, Y. Z. Zhu, Y. J. Li, Y. G. Yao, Y. Zhang, K. Fu, G. Pastel, C. F. Lin, Y. F. Mo, E. D. Wachsman and L. B. Hu, *Adv. Mater.*, 2017, 29.
22 H. Y. Huo, Y. Chen, R. Y. Li, N. Zhao, J. Luo, J. G. P. da Silva, R. Mucke, P. Kaghazchi, X. X. Guo and X. L. Sun, *Energy Environ. Sci.*, 2020, **13**, 127–134.
23 H. H. Xu, Y. T. Li, A. J. Zhou, N. Wu, S. Xin, Z. Y. Li and J. B. Goodenough, *Nano Lett.*, 2018, **18**, 7414–7418.
24 K. Yan, Z. D. Lu, H. W. Lee, F. Xiong, P. C. Hsu, Y. Z. Li, J. Zhao, S. Chu and Y. Cui, *Nat. Energy*, 2016, **1**, 16010.
25 G. Crabtree, *Science*, 2019, **366**, 422–424.
26 J. Tippens, J. C. Miers, A. Afshar, J. A. Lewis, F. J. Q. Cortes, H. P. Qiao, T. S. Marchese, C. V. Di Leo, C. Saldana and M. T. McDowell, *ACS Energy Lett.*, 2019, **4**, 1475–1483.
27 A. S. Westover, N. J. Dudney, R. L. Sacci and S. Kalnaus, *ACS Energy Lett.*, 2019, **4**, 651–655.
28 J. B. Bates, N. J. Dudney, B. Neudecker, A. Ueda and C. D. Evans, *Solid State Ionics*, 2000, **135**, 33–45.
29 Y. Z. Zhu, X. F. He and Y. F. Mo, *ACS Appl. Mater. Interfaces*, 2015, **7**, 23685–23693.
30 J. B. Bates, N. J. Dudney, G. R. Gruzalski, R. A. Zuhr, A. Choudhury, C. F. Luck and J. D. Robertson, *J. Power Sources*, 1993, **43**, 103–110.
31 J. C. Li, C. Ma, M. F. Chi, C. D. Liang and N. J. Dudney, *Adv. Energy Mater.*, 2015, 5.
32 J. Kasemchainan, S. Zekoll, D. S. Jolly, Z. Y. Ning, G. O. Hartley, J. Marrow and P. G. Bruce, *Nat. Mater.*, 2019, **18**, 1105–1111.
33 S. Wang, Y. B. Zhang, X. Zhang, T. Liu, Y. H. Lin, Y. Shen, L. L. Li and C. W. Nan, *ACS Appl. Mater. Interfaces*, 2018, **10**, 42279–42285.
34 D. Y. Cheng, T. A. Wynn, X. F. Wang, S. Wang, M. H. Zhang, R. Shimizu, S. Bai, H. Nguyen, C. C. Fang, M. C. Kim, W. K. Li, B. Y. Lu, S. J. Kim and Y. S. Meng, *Joule*, 2020, **4**, 2484–2500.
35 M. Wang, J. B. Wolfenstine and J. Sakamoto, *Electrochim. Acta*, 2019, **296**, 842–847.
36 K. H. Chen, K. N. Wood, E. Kazyak, W. S. LePage, A. L. Davis, A. J. Sanchez and N. P. Dasgupta, *J. Mater. Chem. A*, 2017, **5**, 11671–11681.

 